

# Large-scale synthesis of low-cost 2D metal–organic frameworks for highly selective photocatalytic CO<sub>2</sub> reduction

Ning-Yu Huang<sup>1,2,3,4</sup>, Zhen-Yu Chen<sup>1,2,3,4</sup>, Fei-Long Hu<sup>1,2,3,4</sup>, Chun-Yan Shang<sup>1,2,3,4</sup>, Wenjuan Wang<sup>1,2,3,4</sup>, Jia-Run Huang<sup>6</sup>, Chuan Zhou<sup>1,3</sup>, Lei Li<sup>1,3</sup>, and Qiang Xu<sup>1,2,3,4,5</sup> (✉)

<sup>1</sup> Shenzhen Key Laboratory of Micro/Nano-Porous Functional Materials (SKLPM), Southern University of Science and Technology, Shenzhen 518055, China

<sup>2</sup> Department of Chemistry, Southern University of Science and Technology, Shenzhen 518055, China

<sup>3</sup> Department of Materials Science and Engineering, Southern University of Science and Technology, Shenzhen 518055, China

<sup>4</sup> SUSTech-Kyoto University Advanced Energy Materials Joint Innovation Laboratory (SKAEM-JIL), Southern University of Science and Technology, Shenzhen 518055, China

<sup>5</sup> Key University Laboratory of Highly Efficient Utilization of Solar Energy and Sustainable Development of Guangdong, Southern University of Science and Technology, Shenzhen 518055, China

<sup>6</sup> MOE Key Laboratory of Bioinorganic and Synthetic Chemistry, School of Chemistry, Sun Yat-sen University, Guangzhou 510275, China

© Tsinghua University Press 2023

Received: 7 November 2022 / Revised: 7 December 2022 / Accepted: 8 December 2022

## ABSTRACT

Two-dimensional metal–organic frameworks (2D MOFs), as a new type of 2D materials, have been widely applied in various applications because of their unique structures and exposed active sites. Herein, we reported two low-cost 2D MOFs constructed by a raw chemical succinic acid (SA), M-SA (M = Ni or Co), which served as efficient photocatalysts for the reduction of CO<sub>2</sub> to CO. Taking advantage of the thinness and open metal sites, the ultrathin Ni-SA nanosheets (ca. 3.6 nm) exhibited excellent CO production of 6.96(7) mmol·g<sup>-1</sup>·h<sup>-1</sup> and CO selectivity of 96.6%. Photoelectrochemical tests and theoretical calculations further confirmed the higher charge transfer efficiency and unsaturated metal sites for promoting photocatalytic performances. More importantly, Ni-SA can also be synthesized in large-scale by an energy-saving method under room temperature, strongly suggesting its promising future and potential for practical applications.

## KEYWORDS

two-dimensional metal–organic framework, low-cost, photocatalysis, CO<sub>2</sub> reduction, large-scale synthesis

## 1 Introduction

The rapid increase in CO<sub>2</sub> emissions caused by the overuse of fossil fuels has led to numerous issues in energy and environment [1–7]. The photocatalytic CO<sub>2</sub> reduction reaction (CO<sub>2</sub>RR) driven by free and sustainable solar energy is a promising way for fuel production (such as carbon monoxide, methane, and formic acid, etc.) and carbon neutrality [8–17]. However, because of the inappropriate design and insufficient utilization of active sites in conventional photocatalysts, the performances of most photocatalysts for CO<sub>2</sub> reduction were still far below the practical requirements, highlighting an urgent need for the development of novel photocatalysts with high activities [18].

Metal–organic frameworks (MOFs), as hybrid organic–inorganic materials with high surface areas and designable structures, have emerged as a new class of porous materials for many potential applications [19–27]. In particular, two-dimensional (2D) MOFs or metal–organic layers (MOLs) have received more and more attentions owing to their thinness and unique structural properties [28–30], which were widely used in the fields of photocatalysis [31–34], electrocatalysis [35, 36], and supercapacitor [37], etc. [38]. For example, Yaghi et al. reported a

series of 2D conductive MOFs, namely M-HHTP (M = Cu, Co, and Ni; HHTP = 2,3,6,7,10,11-hexahydroxytriphenylene), which were thoroughly developed and applied in various fields because of their excellent conductivities and catalytic performances [39–41]. By using capping molecules, Lin and coworkers designed a novel Hf-based MOL anchored with both Ru-based photosensitizers and Re-based catalytic sites, exhibiting remarkable activity for CO<sub>2</sub> photoreduction even under natural sunlight [42]. However, most 2D MOFs require either expensive ligands or elaborate design [43, 44], such as HHTP- and TCPP-based (H<sub>2</sub>TCPP = 4,4',4'',4'''-(porphyrin-5,10,15,20-tetrayl) tetrabenzene) 2D MOFs, which hinder the large-scale applications in catalysis and electrochemistry.

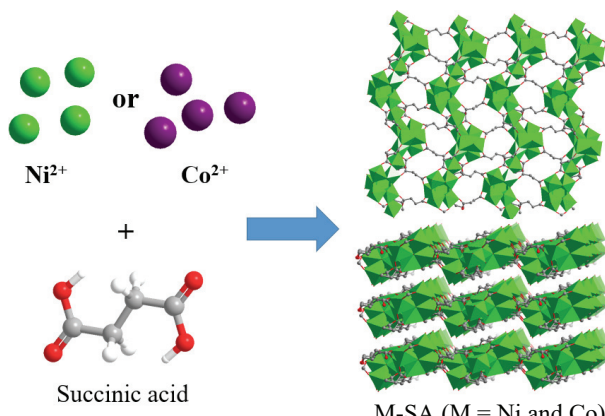
Overall, the synthesis of 2D MOF nanosheets is of great significance but yet a great challenge since the growth of MOFs should be carefully regulated to specific direction and thickness without influencing the lateral growth [45–47]. Herein, using a low-cost raw chemical succinic acid (SA) as ligand, we simply constructed 2D MOFs [M<sub>7</sub>(C<sub>4</sub>H<sub>4</sub>O<sub>4</sub>)<sub>4</sub>(OH)<sub>6</sub>(H<sub>2</sub>O)<sub>3</sub>]·7H<sub>2</sub>O (M-SA, M = Ni or Co) via hydrothermal reactions (Scheme 1), which can be easily exfoliated into nanosheets with the thickness of ca. 3.7 nm. With the help of the unsaturated metal sites, Ni-SA

Address correspondence to xuq@sustech.edu.cn



清华大学出版社  
Tsinghua University Press





**Scheme 1** Schematic illustration of the construction of M-SA (M = Ni or Co).

achieved excellent activity and product selectivity for photocatalytic  $\text{CO}_2$  reduction. Furthermore, Ni-SA can also be synthesized by conveniently stirring under room temperature, making it a promising photocatalyst to meet the large-scale requirement for further applications.

## 2 Results and discussion

Ni-SA was synthesized via simple hydrothermal reaction by using nickel chloride and succinic acid [48]. The phase purity of Ni-SA was confirmed by powder X-ray diffraction (PXRD) patterns (Fig. S1 in the Electronic Supplementary Material (ESM)). According to the crystal structure of Ni-SA, the nickel oxide chains running along the *b* axis are bridged by succinate ions, weaving a layer in [100] facet (Fig. S2(a) in the ESM). Further, these layers are stacked and interacted by hydrogen-bonding from  $\mu_2\text{-OH}$  and coordinated water molecules, instead of connecting covalently or coordinately, making them more conducive to exfoliation (Fig. S2(b) in the ESM). The thickness of a single layer in Ni-SA was measured as 11.7 Å. In the asymmetric unit of Ni-SA, seven Ni ions are presented with octahedral geometry, two of which are coordinated by terminal  $\text{H}_2\text{O}$  molecules. It is worth noting that after removing the coordinated  $\text{H}_2\text{O}$  molecules, the coordination mode of Ni ions can be changed from octahedral to tetragonal-pyramid geometry (Fig. S3 in the ESM), accompanied by the open of unsaturated metal sites.

X-ray photoelectron spectroscopy (XPS) was performed to study the electronic property of Ni-SA. As shown in Fig. S4 in the ESM, broad Ni 2p<sub>3/2</sub> and Ni 2p<sub>1/2</sub> peaks were observed with binding energies of 854.9 and 872.7 eV, respectively, corresponding to the  $\text{Ni}^{2+}$  species. Based on the nitrogen adsorption isotherms at 77 K (Fig. S5 in the ESM), the Brunauer–Emmett–Teller (BET) surface area of Ni-SA was calculated to be 31.88 m<sup>2</sup>·g<sup>-1</sup>, which was similar with the reported 2D MOFs [49, 50], indicating the nonporous structure for bulk Ni-SA. More importantly, Ni-SA exhibited good chemical stability in water under acidic ( $\text{pH} = 2$ ) and basic ( $\text{pH} = 13$ ) conditions for at least 24 h according to the PXRD patterns (Fig. S1 in the ESM), which met the needs for photocatalysis.

To reveal its 2D characteristics, the morphology of Ni-SA was further characterized by scanning electron microscopy (SEM), transmission electron microscopy (TEM), and atomic force microscopy (AFM). SEM image (Fig. 1(a)) revealed that the bulk Ni-SA was rod-like nanocrystals with the size of ca. 100 nm × 300 nm. Due to its well-defined layered structure, Ni-SA can be easily exfoliated into self-supporting two-dimensional MOF nanosheets via sonication, showing typical Tyndall effect of the colloidal suspension (inset of Fig. 1(b)). According to the TEM and AFM images (Figs. 1(b) and 1(c)), as well as the height

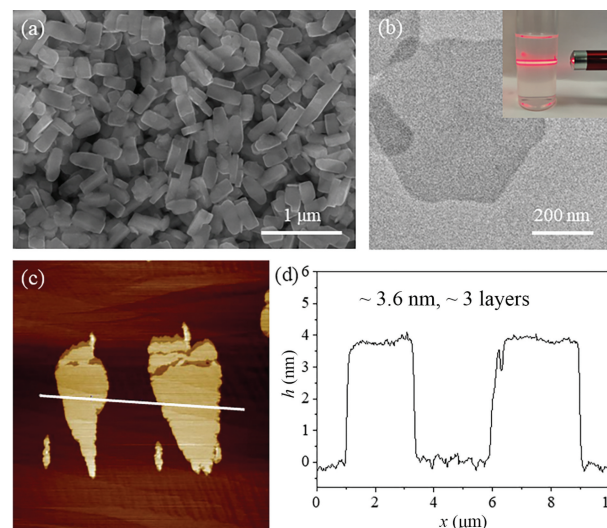


**Figure 1** (a) SEM image, (b) TEM image (inset: an optical image showing the Tyndall effect), (c) AFM image, and (d) the corresponding height profile of Ni-SA nanosheets.

profiles (Fig. 1(d)) derived from AFM, the Ni-SA nanosheets displayed ultrathin morphology with the thickness of 3.6 nm (~ 3 layers) and the lateral size up to a few micrometers.

To further explore the family of metal succinate frameworks, the Co-based analogue Co-SA [51], isostructural to Ni-SA, was also constructed via hydrothermal reaction. The purity and morphology of Co-SA were confirmed by PXRD patterns (Fig. S6 in the ESM) and SEM image (Fig. S7 in the ESM). Furthermore, XPS spectrum of Co-SA showed that the metal ions were all divalent (Fig. S8 in the ESM). Similar to Ni-SA, after sonication, Co-SA can be conveniently exfoliated into ultrathin nanosheets with the thickness of ca. 3.5 nm (Figs. S9 and S10 in the ESM), further confirming the 2D structure of M-SA.

Taking advantages of the ultrathin nanosheets and unsaturated metal sites, the photocatalytic  $\text{CO}_2$  reduction performances of Ni-SA and Co-SA nanosheets were evaluated under LED irradiation ( $\lambda > 410$  nm) in acetonitrile/water (v/v = 4:1), using triethanolamine (TEOA) as a sacrificial agent and  $[\text{Ru}(\text{phen})_3]\text{Cl}_2$  (phen = 1,10-phenanthroline) as a photosensitizer. The gas-phase products were detected by gas chromatography (Fig. S11 in the ESM). For the optimization of the best amount of photocatalyst, the performances of different amounts of Ni-SA were measured under the same conditions (Fig. S12 in the ESM). The catalytic performances of photocatalytic  $\text{CO}_2$  reduction increased with the amount of catalyst increasing up to 1 mg and decreased with the higher catalyst feedings. On the one hand, the lower catalyst feeding can cause the lack of active sites, leading to poor performances. On the other hand, considering the 2D structure of Ni-SA, excessive catalysts may cause the overlap of the ultrathin nanosheets, resulting in the insufficient utilization of the active sites and lower the photocatalytic activity, which indicated the benefits from ultrathin morphology.

After irradiated for 4 h, the amount of CO and  $\text{H}_2$  increased linearly with the irradiation time (Fig. 2(a)). The Ni-SA nanosheets exhibited excellent CO production rates of 6.96(7) mmol·g<sup>-1</sup>·h<sup>-1</sup>, accompanied with a small amount of  $\text{H}_2$  (0.245(6) mmol·g<sup>-1</sup>·h<sup>-1</sup>), indicating the high CO selectivity (ca. 96.6%). In comparison, the CO and  $\text{H}_2$  production rates of Co-SA were 2.95(9) and 1.05(2) mmol·g<sup>-1</sup>·h<sup>-1</sup>, respectively, showing lower activity and product selectivity. No other liquid products were generated for both photocatalysts, which was confirmed by <sup>1</sup>H nuclear magnetic resonance (<sup>1</sup>H NMR, Fig. S13 in the ESM). Furthermore, the apparent quantum yield (AQY) of Ni-SA was

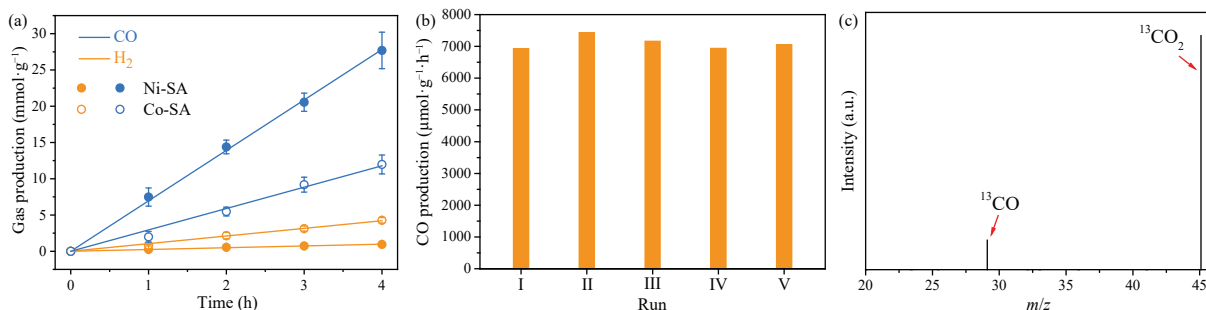


**Figure 2** (a) CO and H<sub>2</sub> production rates of photocatalytic CO<sub>2</sub> reduction by using Ni-SA and Co-SA as photocatalysts. (b) CO production rates of cyclic photocatalytic CO<sub>2</sub> reduction reactions by using Ni-SA as catalyst. (c) Mass spectra of the products of photocatalytic CO<sub>2</sub> reduction by using <sup>13</sup>CO<sub>2</sub> as the gas source.

determined as 2.72% at 420 nm for CO production, which was comparable among the reported photocatalysts (Table S1 in the ESM).

Considering the significance of recyclability for photocatalysts, the cyclic experiments of photocatalytic CO<sub>2</sub> reduction were conducted for Ni-SA nanosheets. By adding additional photosensitizers and sacrificial agents after each round, reproducible photocatalytic activities were achieved for at least five cycles (Fig. 2(b)), indicating the outstanding stability of Ni-SA. Additionally, the intactness of Ni-SA was also confirmed by the PXRD patterns (Fig. S14 in the ESM), SEM image (Fig. S15 in the ESM), and N<sub>2</sub> adsorption isotherms (Fig. S5 in the ESM), giving similar BET surface areas for Ni-SA before (31.88 m<sup>2</sup>·g<sup>-1</sup>) and after (29.18 m<sup>2</sup>·g<sup>-1</sup>) photocatalysis.

To further verify the origin of generated CO, the isotope labeling experiments were conducted by using <sup>13</sup>CO<sub>2</sub> as carbon source. In the presence of <sup>13</sup>CO<sub>2</sub> (*m/z* = 45), <sup>13</sup>CO (*m/z* = 29) was clearly detected by gas chromatography-mass spectrometry (GC-MS, Fig. 2(c)), indicating that CO originated from gaseous CO<sub>2</sub> reactant. Furthermore, control experiments with no catalyst, photosensitizer, sacrificial agent, CO<sub>2</sub>, or light were carried out under the same conditions otherwise as the complete photocatalytic system (Fig. S16 and Table S2 in the ESM). Negligible products can be detected, demonstrating the significance of each condition for photocatalytic process. In particular, similar to the control experiment without the catalysts, a mixture of NiCl<sub>2</sub> and succinic acid as catalyst can only produce CO with very low activity, implying the necessity of the coordination network of Ni-SA for photocatalysis. To exclude the influence of extra metal ions or nanoparticles, the content of Ni and Co was confirmed by inductively coupled plasma optical emission spectrometry (ICP-OES) as 35.59% and 36.95%, respectively (Table S3 in the ESM), which was consistent with their theoretical values based on the crystal structures (35.50% and 35.60%), indicating the intrinsic catalytic activity for Ni-SA and Co-SA.

To investigate the charge transfer efficiency of different photocatalysts, photoluminescence (PL) spectra and electrochemical impedance spectroscopy (EIS) of Ni-SA and Co-SA were measured under the identical conditions of photocatalytic

experiments. As shown in Fig. S17 in the ESM, under the excitation at 500 nm, the characteristic peak of Ru(phen)<sub>3</sub>Cl<sub>2</sub> at 590 nm decreased after the addition of both Ni-SA and Co-SA, indicating the efficient charge transfer process for both catalysts. The lower PL emission for Ni-SA further demonstrated the higher charge transfer efficiency, which was consistent with the performances of photocatalytic CO<sub>2</sub> reduction. This was further supported by the EIS spectra, in which Ni-SA showed a smaller semicircle in the Nyquist plots (Fig. S18 in the ESM), implying lower charge transfer resistance, more timely transport of photogenerated electrons and more efficient separation of photoexcited electron-hole pairs.

To further explore the reaction mechanism of photocatalytic CO<sub>2</sub> reduction, density functional theory (DFT) calculations were carried out to evaluate the adsorption free energies of the reaction intermediates (\*CO and \*COOH) for Ni-SA and Co-SA (Fig. S19 in the ESM). The unsaturated metal sites can serve as binding sites for reaction intermediates and accomplish CO<sub>2</sub>-to-CO reduction. As shown in Fig. 3(a), although Co-SA lowered the reaction free energy of the potential limiting step (\* + CO<sub>2</sub> + (H<sup>+</sup> + e<sup>-</sup>) → \*COOH) in CO<sub>2</sub> reduction compared to Ni-SA, the thermodynamically unfavorable CO desorption for Co-SA resulted in the CO poisoning of active sites and greatly impeded its catalytic performance. More importantly, Co-SA showed lower reaction free energy for hydrogen evolution reaction (HER, Fig. S20 in the ESM), indicating the occurrence of more competitive HER and lower CO selectivity in Co-SA. According to the literature, the difference between potentials of limiting step for H<sub>2</sub> evolution and CO<sub>2</sub> reduction (denoted as U<sub>L</sub>(CO<sub>2</sub>) – U<sub>L</sub>(H<sub>2</sub>)) can be calculated to evaluate the selectivity of CO<sub>2</sub> reduction over HER [52, 53]. Compared to Co-SA (-0.34 V), Ni-SA showed a significantly more positive value of U<sub>L</sub>(CO<sub>2</sub>) – U<sub>L</sub>(H<sub>2</sub>) (-0.13 V, Fig. 3(b)), which can account for the higher activity and product selectivity of Ni-SA.

As the basic premise for practical application, large-scale and energy-saving synthesis of catalysts is of great significance but challenging for most 2D MOF materials. By adding the aqueous solution containing metal ions dropwise into ligand solution, Ni-SA can also be conveniently synthesized through simple stirring under room temperature, namely Ni-SA-RT (RT = room temperature), with the yield of ca. 95.3% based on Ni. Compared

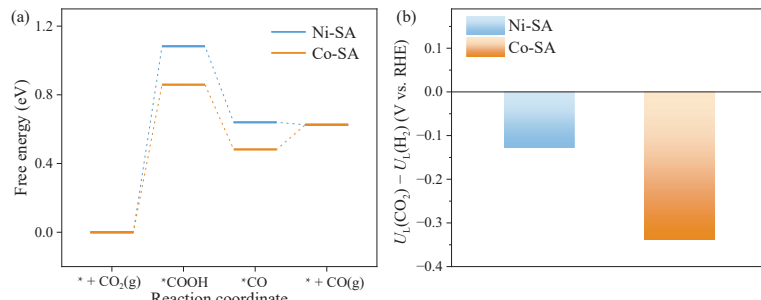


**Figure 3** (a) Free-energy diagrams of reducing CO<sub>2</sub> to CO for Ni-SA and Co-SA. (b) Difference in limiting potentials for CO<sub>2</sub> reduction and H<sub>2</sub> evolution.

with Ni-SA, the purity and oxidation state of Ni-SA-RT were confirmed by PXRD patterns (Fig. S21 in the ESM) and XPS spectra (Fig. S22 in the ESM), further identifying the same material obtained via different methods. According to the photocatalytic CO<sub>2</sub> reduction experiments (Fig. 4), the CO production of 6.93 mmol·g<sup>-1</sup>·h<sup>-1</sup> and CO selectivity of 97.6% were achieved by Ni-SA-RT, which not only confirmed its outstanding performance, but also illustrated the successful combination of convenient synthesis and high activity for Ni-SA-RT.

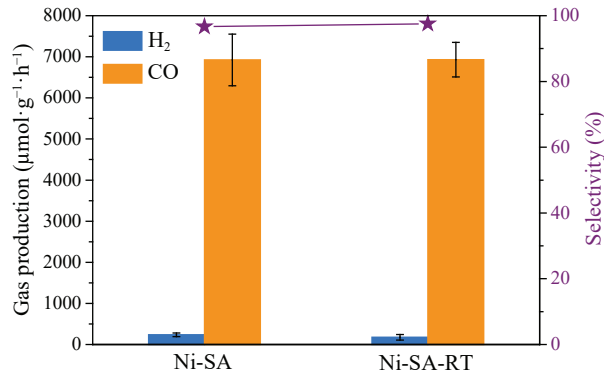


**Figure 4** Comparison of the performances of photocatalytic CO<sub>2</sub> reduction for Ni-SA and Ni-SA-RT.

### 3 Conclusions

In summary, by using a low-cost ligand succinic acid, two isostructural 2D MOFs M-SA (M = Ni or Co) have been synthesized and demonstrated to be efficient photocatalysts for photocatalytic CO<sub>2</sub>-to-CO reduction. Owing to the intrinsic 2D structure, Ni-SA can be conveniently exfoliated into ultrathin nanosheets with the thickness of ca. 3.6 nm. Taking advantage of the unsaturated metal sites, the ultrathin Ni-SA nanosheets exhibited excellent activity and selectivity for photocatalytic CO<sub>2</sub> reduction to CO. To meet the requirements and needs of further applications, large-scale and energy-saving synthesis of Ni-SA can also be achieved by simply stirring under room temperature, highlighting the enormous potential for practical applications. Considering the significance of 2D materials, the successful construction and application of M-SA in this work provide a new pathway in fabricating and developing efficient 2D MOF-based catalysts.

### Acknowledgements

This work was supported by Shenzhen Key Laboratory of Micro/Nano-Porous Functional Materials (SKLPM) (No. ZDSYS20210709112802010) and China Postdoctoral Science Foundation (No. 2022M711483).

**Electronic Supplementary Material:** Supplementary material (synthesis, structural characterization, PXRD, XPS, SEM, AFM, and photocatalytic experiments) is available in the online version of this article at <https://doi.org/10.1007/s12274-023-5405-8>.

### References

- Huang, Z.; Grim, R. G.; Schaidle, J. A.; Tao, L. The economic outlook for converting CO<sub>2</sub> and electrons to molecules. *Energy Environ. Sci.* **2021**, *14*, 3664–3678.
- Jiao, X. C.; Zheng, K.; Liang, L.; Li, X. D.; Sun, Y. F.; Xie, Y. Fundamentals and challenges of ultrathin 2D photocatalysts in boosting CO<sub>2</sub> photoreduction. *Chem. Soc. Rev.* **2020**, *49*, 6592–6604.
- Liang, J.; Wu, Q.; Huang, Y. B.; Cao, R. Reticular frameworks and their derived materials for CO<sub>2</sub> conversion by thermo-catalysis. *EnergyChem* **2021**, *3*, 100064.
- Navarro-Jaén, S.; Virginie, M.; Bonin, J.; Robert, M.; Wojcieszak, R.; Khodakov, A. Y. Highlights and challenges in the selective reduction of carbon dioxide to methanol. *Nat. Rev. Chem.* **2021**, *5*, 564–579.
- Chang, X. X.; Wang, T.; Gong, J. L. CO<sub>2</sub> photo-reduction: Insights into CO<sub>2</sub> activation and reaction on surfaces of photocatalysts. *Energy. Environ. Sci.* **2016**, *9*, 2177–2196.
- Sun, X. H.; Sun, L.; Li, G. N.; Tuo, Y. X.; Ye, C. L.; Yang, J. R.; Low, J.; Yu, X.; Bitter, J. H.; Lei, Y. P. et al. Phosphorus tailors the d-band center of copper atomic sites for efficient CO<sub>2</sub> photoreduction under visible-light irradiation. *Angew. Chem., Int. Ed.* **2022**, *61*, e202207677.
- Zhang, R. Z.; Wu, B. Y.; Li, Q.; Lu, L. L.; Shi, W.; Cheng, P. Design strategies and mechanism studies of CO<sub>2</sub> electroreduction catalysts based on coordination chemistry. *Coord. Chem. Rev.* **2020**, *422*, 213436.
- Wang, Y.; Huang, N. Y.; Shen, J. Q.; Liao, P. Q.; Chen, X. M.; Zhang, J. P. Hydroxide ligands cooperate with catalytic centers in metal–organic frameworks for efficient photocatalytic CO<sub>2</sub> reduction. *J. Am. Chem. Soc.* **2018**, *140*, 38–41.
- Boutin, E.; Merakeb, L.; Ma, B.; Boudy, B.; Wang, M.; Bonin, J.; Anxolabéhère-Mallart, E.; Robert, M. Molecular catalysis of CO<sub>2</sub> reduction: Recent advances and perspectives in electrochemical and light-driven processes with selected Fe, Ni and Co aza macrocyclic and polypyridine complexes. *Chem. Soc. Rev.* **2020**, *49*, 5772–5809.
- Zhang, B. B.; Sun, L. C. Artificial photosynthesis: Opportunities and challenges of molecular catalysts. *Chem. Soc. Rev.* **2019**, *48*, 2216–2264.
- Wang, Y. O.; Chen, E. Q.; Tang, J. W. Insight on reaction pathways of photocatalytic CO<sub>2</sub> conversion. *ACS Catal.* **2022**, *12*, 7300–7316.
- Kreft, S.; Wei, D.; Junge, H.; Beller, M. Recent advances on TiO<sub>2</sub>-based photocatalytic CO<sub>2</sub> reduction. *EnergyChem* **2020**, *2*, 100044.
- Xiong, X. Y.; Zhao, Y. F.; Shi, R.; Yin, W. J.; Zhao, Y. X.; Waterhouse, G. I. N.; Zhang, T. R. Selective photocatalytic CO<sub>2</sub> reduction over Zn-based layered double hydroxides containing tri or tetravalent metals. *Sci. Bull.* **2020**, *65*, 987–994.
- Wang, Y.; Zhang, Z. Z.; Zhang, L. N.; Luo, Z. B.; Shen, J. N.; Lin, H. X.; Long, J. L.; Wu, J. C. S.; Fu, X. Z.; Wang, X. X. Visible-light driven overall conversion of CO<sub>2</sub> and H<sub>2</sub>O to CH<sub>4</sub> and O<sub>2</sub> on 3D-SiC@2D-MoS<sub>2</sub> heterostructure. *J. Am. Chem. Soc.* **2018**, *140*, 14595–14598.
- Wang, G.; Chen, Z.; Wang, T.; Wang, D. S.; Mao, J. J. P. and Cu dual sites on graphitic carbon nitride for photocatalytic CO<sub>2</sub> reduction to hydrocarbon fuels with high C<sub>2</sub>H<sub>6</sub> evolution. *Angew. Chem., Int. Ed.* **2022**, *61*, e202210789.
- Ou, H. H.; Ning, S. B.; Zhu, P.; Chen, S. H.; Han, A. L.; Kang, Q.; Hu, Z. F.; Ye, J. H.; Wang, D. S.; Li, Y. D. Carbon nitride photocatalysts with integrated oxidation and reduction atomic active centers for improved CO<sub>2</sub> conversion. *Angew. Chem., Int. Ed.* **2022**, *61*, e202206579.
- Huang, G. C.; Niu, Q.; He, Y. X.; Tian, J. J.; Gao, M. B.; Li, C. Y.; An, N.; Bi, J. H.; Zhang, J. W. Spatial confinement of copper single atoms into covalent triazine-based frameworks for highly efficient and selective photocatalytic CO<sub>2</sub> reduction. *Nano Res.* **2022**, *15*, 8001–8009.
- Luo, Y. H.; Dong, L. Z.; Liu, J.; Li, S. L.; Lan, Y. Q. From molecular metal complex to metal–organic framework: The CO<sub>2</sub> reduction photocatalysts with clear and tunable structure. *Coord. Chem. Rev.* **2019**, *390*, 86–126.
- Li, D. D.; Kassymova, M.; Cai, X. C.; Zang, S. Q.; Jiang, H. L. Photocatalytic CO<sub>2</sub> reduction over metal–organic framework-based materials. *Coord. Chem. Rev.* **2020**, *412*, 213262.
- Li, D. D.; Xu, H. Q.; Jiao, L.; Jiang, H. L. Metal–organic frameworks for catalysis: State of the art, challenges, and opportunities. *EnergyChem* **2019**, *1*, 100005.
- Rao, H.; Schmidt, L. C.; Bonin, J.; Robert, M. Visible-light-driven methane formation from CO<sub>2</sub> with a molecular iron catalyst. *Nature* **2017**, *548*, 74–77.
- Jiang, Z.; Xu, X. H.; Ma, Y. H.; Cho, H. S.; Ding, D.; Wang, C.; Wu, J.; Oleynikov, P.; Jia, M.; Cheng, J. et al. Filling metal–organic

- framework mesopores with  $\text{TiO}_2$  for  $\text{CO}_2$  photoreduction. *Nature* **2020**, *586*, 549–554.
- [23] Trickett, C. A.; Helal, A.; Al-Maythalony, B. A.; Yamani, Z. H.; Cordova, K. E.; Yaghi, O. M. The chemistry of metal–organic frameworks for  $\text{CO}_2$  capture, regeneration and conversion. *Nat. Rev. Mater.* **2017**, *2*, 17045.
- [24] Huang, N. Y.; Zhang, X. W.; Xu, Y. Z.; Liao, P. Q.; Chen, X. M. A local hydrophobic environment in a metal–organic framework for boosting photocatalytic  $\text{CO}_2$  reduction in the presence of water. *Chem. Commun.* **2019**, *55*, 14781–14784.
- [25] Kajiwara, T.; Fujii, M.; Tsujimoto, M.; Kobayashi, K.; Higuchi, M.; Tanaka, K.; Kitagawa, S. Photochemical reduction of low concentrations of  $\text{CO}_2$  in a porous coordination polymer with a ruthenium(II)–CO complex. *Angew. Chem., Int. Ed.* **2016**, *55*, 2697–2700.
- [26] Cheng, X. M.; Dao, X. Y.; Wang, S. Q.; Zhao, J.; Sun, W. Y. Enhanced photocatalytic  $\text{CO}_2$  reduction activity over  $\text{NH}_2\text{-MIL}-125(\text{Ti})$  by facet regulation. *ACS Catal.* **2021**, *11*, 650–658.
- [27] Zhang, H. B.; Wei, J.; Dong, J. C.; Liu, G. G.; Shi, L.; An, P. F.; Zhao, G. X.; Kong, J. T.; Wang, X. J.; Meng, X. G. et al. Efficient visible-light-driven carbon dioxide reduction by a single-atom implanted metal–organic framework. *Angew. Chem., Int. Ed.* **2016**, *55*, 14310–14314.
- [28] Liu, J. J.; Song, X. Y.; Zhang, T.; Liu, S. Y.; Wen, H. R.; Chen, L. 2D conductive metal–organic frameworks: An emerging platform for electrochemical energy storage. *Angew. Chem., Int. Ed.* **2021**, *60*, 5612–5624.
- [29] Lin, Y.; Li, W. H.; Wen, Y. Y.; Wang, G. E.; Ye, X. L.; Xu, G. Layer-by-layer growth of preferred-oriented MOF thin film on nanowire array for high-performance chemiresistive sensing. *Angew. Chem., Int. Ed.* **2021**, *60*, 25758–25761.
- [30] Li, Q.; Lu, L. L.; Liu, J. W.; Shi, W.; Cheng, P. Two-dimensional bimetallic coordination polymers as bifunctional evolved electrocatalysts for enhanced oxygen evolution reaction and urea oxidation reaction. *J. Energy Chem.* **2021**, *63*, 230–238.
- [31] Xia, Y. S.; Tang, M. Z.; Zhang, L.; Liu, J.; Jiang, C.; Gao, G. K.; Dong, L. Z.; Xie, L. G.; Lan, Y. Q. Tandem utilization of  $\text{CO}_2$  photoreduction products for the carbonylation of aryl iodides. *Nat. Commun.* **2022**, *13*, 2964.
- [32] Yang, W.; Wang, H. J.; Liu, R. R.; Wang, J. W.; Zhang, C.; Li, C.; Zhong, D. C.; Lu, T. B. Tailoring crystal facets of metal–organic layers to enhance photocatalytic activity for  $\text{CO}_2$  reduction. *Angew. Chem., Int. Ed.* **2021**, *60*, 409–414.
- [33] Wang, J. W.; Qiao, L. Z.; Nie, H. D.; Huang, H. H.; Li, Y.; Yao, S.; Liu, M.; Zhang, Z. M.; Kang, Z. H.; Lu, T. B. Facile electron delivery from graphene template to ultrathin metal–organic layers for boosting  $\text{CO}_2$  photoreduction. *Nat. Commun.* **2021**, *12*, 813.
- [34] Han, B.; Ou, X. W.; Deng, Z. Q.; Song, Y.; Tian, C.; Deng, H.; Xu, Y. J.; Lin, Z. Nickel metal–organic framework monolayers for photoreduction of diluted  $\text{CO}_2$ : Metal-node-dependent activity and selectivity. *Angew. Chem., Int. Ed.* **2018**, *57*, 16811–16815.
- [35] Yi, J. D.; Xie, R. K.; Xie, Z. L.; Chai, G. L.; Liu, T. F.; Chen, R. P.; Huang, Y. B.; Cao, R. Highly selective  $\text{CO}_2$  electroreduction to  $\text{CH}_4$  by *in situ* generated  $\text{Cu}_2\text{O}$  single-type sites on a conductive MOF: Stabilizing key intermediates with hydrogen bonding. *Angew. Chem., Int. Ed.* **2020**, *59*, 23641–23648.
- [36] Miner, E. M.; Fukushima, T.; Sheberla, D.; Sun, L.; Surendranath, Y.; Dincă, M. Electrochemical oxygen reduction catalysed by  $\text{Ni}_3(\text{hexaiminotriphenylene})_2$ . *Nat. Commun.* **2016**, *7*, 10942.
- [37] Sheberla, D.; Bachman, J. C.; Elias, J. S.; Sun, C. J.; Shao-Horn, Y.; Dincă, M. Conductive MOF electrodes for stable supercapacitors with high areal capacitance. *Nat. Mater.* **2017**, *16*, 220–224.
- [38] Shinde, S. S.; Lee, C. H.; Jung, J. Y.; Wagh, N. K.; Kim, S. H.; Kim, D. H.; Lin, C.; Lee, S. U.; Lee, J. H. Unveiling dual-linkage 3D hexaiminobenzene metal–organic frameworks towards long-lasting advanced reversible Zn–air batteries. *Energy Environ. Sci.* **2019**, *12*, 727–738.
- [39] Hmadeh, M.; Lu, Z.; Liu, Z.; Gádára, F.; Furukawa, H.; Wan, S.; Augustyn, V.; Chang, R.; Liao, L.; Zhou, F. et al. New porous crystals of extended metal–catecholates. *Chem. Mater.* **2012**, *24*, 3511–3513.
- [40] Yao, M. S.; Zheng, J. J.; Wu, A. Q.; Xu, G.; Nagarkar, S. S.; Zhang, G.; Tsujimoto, M.; Sakaki, S.; Horike, S.; Otake, K. et al. A dual-ligand porous coordination polymer chemiresistor with modulated conductivity and porosity. *Angew. Chem., Int. Ed.* **2020**, *59*, 172–176.
- [41] Huang, N. Y.; He, H.; Liu, S. J.; Zhu, H. L.; Li, Y. J.; Xu, J.; Huang, J. R.; Wang, X.; Liao, P. Q.; Chen, X. M. Electrostatic attraction-driven assembly of a metal–organic framework with a photosensitizer boosts photocatalytic  $\text{CO}_2$  reduction to CO. *J. Am. Chem. Soc.* **2021**, *143*, 17424–17430.
- [42] Lan, G. X.; Li, Z.; Veroneau, S. S.; Zhu, Y. Y.; Xu, Z. W.; Wang, C.; Lin, W. B. Photosensitizing metal–organic layers for efficient sunlight-driven carbon dioxide reduction. *J. Am. Chem. Soc.* **2018**, *140*, 12369–12373.
- [43] Zuo, Q.; Liu, T. T.; Chen, C. S.; Ji, Y.; Gong, X. Q.; Mai, Y. Y.; Zhou, Y. F. Ultrathin metal–organic framework nanosheets with ultrahigh loading of single Pt atoms for efficient visible-light-driven photocatalytic  $\text{H}_2$  evolution. *Angew. Chem., Int. Ed.* **2019**, *58*, 10198–10203.
- [44] Meng, Z.; Mirica, K. A. Two-dimensional d–π conjugated metal–organic framework based on hexahydroxytrinaphthylene. *Nano Res.* **2021**, *14*, 369–375.
- [45] Chakraborty, G.; Park, I. H.; Medishetty, R.; Vittal, J. J. Two-dimensional metal–organic framework materials: Synthesis, structures, properties and applications. *Chem. Rev.* **2021**, *121*, 3751–3891.
- [46] Wang, M. C.; Dong, R. H.; Feng, X. L. Two-dimensional conjugated metal–organic frameworks (2D c-MOFs): Chemistry and function for MOFtronics. *Chem. Soc. Rev.* **2021**, *50*, 2764–2793.
- [47] Lahiri, N.; Lotfizadeh, N.; Tsuchikawa, R.; Deshpande, V. V.; Louie, J. Hexaaminobenzene as a building block for a family of 2D coordination polymers. *J. Am. Chem. Soc.* **2017**, *139*, 19–22.
- [48] Guillou, N.; Livage, C.; van Beek, W.; Noguès, M.; Férey, G. A layered nickel succinate with unprecedented hexanickel units: Structure elucidation from powder-diffraction data, and magnetic and sorption properties. *Angew. Chem., Int. Ed.* **2003**, *42*, 643–647.
- [49] Jiang, Y.; Oh, I.; Joo, S. H.; Seo, Y. S.; Lee, S. H.; Seong, W. K.; Kim, Y. J.; Hwang, J.; Kwak, S. K.; Yoo, J. W. et al. Synthesis of a copper 1,3,5-triamino-2,4,6-benzenetriol metal–organic framework. *J. Am. Chem. Soc.* **2020**, *142*, 18346–18354.
- [50] Banda, H.; Dou, J. H.; Chen, T. Y.; Libretto, N. J.; Chaudhary, M.; Bernard, G. M.; Miller, J. T.; Michaelis, V. K.; Dincă, M. High-capacitance pseudocapacitors from  $\text{Li}^+$  ion intercalation in nonporous, electrically conductive 2D coordination polymers. *J. Am. Chem. Soc.* **2021**, *143*, 2285–2292.
- [51] Forster, P. M.; Burbank, A. R.; O’Sullivan, M. C.; Guillou, N.; Livage, C.; Férey, G.; Stock, N.; Cheetham, A. K. Single-crystal characterization of  $\text{Co}_7(\text{OH})_6(\text{H}_2\text{O})_3(\text{C}_4\text{H}_4\text{O}_4)_4 \cdot 7\text{H}_2\text{O}$ ; a new cobalt succinate identified through high-throughput synthesis. *Solid State Sci.* **2005**, *7*, 1549–1555.
- [52] Li, X. G.; Bi, W. T.; Chen, M. L.; Sun, Y. X.; Ju, H. X.; Yan, W. S.; Zhu, J. F.; Wu, X. J.; Chu, W. S.; Wu, C. Z. et al. Exclusive  $\text{Ni-N}_4$  sites realize near-unity CO selectivity for electrochemical  $\text{CO}_2$  reduction. *J. Am. Chem. Soc.* **2017**, *139*, 14889–14892.
- [53] Kim, D.; Xie, C. L.; Becknell, N.; Yu, Y.; Karamad, M.; Chan, K. R.; Crumlin, E. J.; Nørskov, J. K.; Yang, P. D. Electrochemical activation of  $\text{CO}_2$  through atomic ordering transformations of AuCu nanoparticles. *J. Am. Chem. Soc.* **2017**, *139*, 8329–8336.